Impact of strain on Si and Sn incorporation in (Si)GeSn alloys by STEM analyses

Florian Castioni, Loïc Henry, Lara Casiez, Nicolas Bernier, Vincent Reboud, Jérémie Chrétien, Nicolas Pauc, Vincent Calvo, Jérôme Richy, Audrey Jannaud, et al.

Impact of strain on Si and Sn incorporation in (Si)GeSn alloys by STEM analyses

Florian Castioni[1*], Loïc Henry[2], Lara Casiez[1], Nicolas Bernier[1], Vincent Reboud[1], Audrey Jannaud[1], Vincent Delaye[1], Eric Robin[3], Jean-Michel Hartmann[1], Pascale Bayle-Guillemaud[3]

[1] Univ. Grenoble Alpes, CEA, LETI, 38000 Grenoble, France

[2] STMicroelectronics, 12 Rue Jules Horowitz, 38019 Grenoble

[3] Univ. Grenoble Alpes, CEA, IRIG, 38000 Grenoble, France

* Corresponding author: florian.castioni@cea.fr (F. Castioni)

Abstract:

The impact of device structure on the properties of CVD-grown (Si)GeSn heterostructures was assessed thanks to scanning transmission electron microscopy (STEM) at the nanometer scale. Quantitative energy dispersive x-ray spectroscopy (EDX) together with precession electron diffraction (PED) and geometrical phase analysis (GPA) were performed to probe the chemical and structural properties of the different layers. The results presented in this paper demonstrated the advantages of a multilayer structure, with successive layers grown at decreasing temperature in order to gradually accommodate the in-plane lattice parameter and incorporate more and more Sn into the stack. It was shown how the GeSn emissive layer could be manufactured with low plastic deformation and high relaxation rate, necessary for better emissive performances. SiGeSn alloys

used as confinement barriers around the emissive layer were also investigated. For such thin layers, we showed the importance of the starting lattice parameter (SLP) before the growth on their composition. Indeed, higher SLPs resulted, for the very same process conditions, into higher Sn contents and lower Si contents. The interest of combining EDX, which was accurate enough to detect slight chemical concentration variations, and GPA, for local strain analyses, was clearly demonstrated. Present results will be very useful to predict and control the bandgap and structural quality of (Si)GeSn materials and in turn the device properties.

Keywords:

1. Introduction

Si photonics has garnered a great deal of interest during the last decade, the aim being to reduce power consumption and increase speed during data transfer. The monolithic integration of light sources on Si a major building block of such devices. III-V semiconductors, the main materials considered for infra-red optical components, present the drawback of being hardly compatible with CMOS technology. Meanwhile, because they are group-IV semiconductors with the same diamond structures than Si, binary GeSn and ternary SiGeSn alloys were identified as serious candidates for such light sources [1–3]. The bandgap of such alloys becomes direct above 8-9% atomic of Sn (for a relaxed material), and can be tuned thanks to Sn and Si concentration and elastic strain variations [1]. It therefore opens up possibilities in the mid infra-red [4–7].

However, the growth of Sn based alloys on Si or Ge substrates is far from being easy. The lattice mismatch between Si, Ge and Sn is large (a_{Si} = 5.431 Å, a_{Ge} = 5.658 Å and a_{Sn} = 6.489 Å) and their melting temperature very different (1414°C for Si, 938°C for Ge and 232°C for Sn). While Si and Ge are miscible in all proportions, it is otherwise not feasible to have more than 1% of Sn in GeSn layers at thermal equilibrium. If the growth of high Sn content (Si)GeSn can be achieved, it requires conditions far from thermodynamic equilibrium (e.g. high growth rates at temperatures less than 350 °C, typically). Such layers will be highly compressively strained even if Ge strain-relaxed buffers on Si are used, and a dramatic segregation of Sn at the surface might occur if the thermal budget is too high [8]. A very careful optimization of the properties of each (Si)GeSn layer is therefore mandatory to obtain high-performance components. We indeed target high amounts of Sn (more than 10%, typically) in optical active layers that should ideally be strain free, to have a more direct bandgap, and as defect-free as possible. Step-graded structures, with a gradual increase of the Sn content from a few % at the bottom to 13%-16% of Sn at the top, were shown to have superior light emission properties stemming from a better crystalline quality (more relaxed and dislocations free emissive layer) and a better incorporation of Sn [9–12]. In addition, SiGeSn barrier layers with larger bandgaps were used to optimize the confinement of charge carriers in the emission layer, with better light emission properties [13,14].

Several studies have focused on the link between the strain state and the incorporation of Sn into GeSn crystals. To a large extent, these studies involve non-local techniques such as x-ray diffraction (XRD), reciprocal space mapping (RSM) or wavelength dispersive x-ray fluorescence (WDXRF) [10,11,15–17]. Due to their relatively low depth resolution, these approaches showed limits in analyzing multilayered structures, with layer compositions which can be quite close or even gradual. Transmission electron microscopy was used in some studies to probe these properties at the nanometer scale, to unambiguously discriminate the chemical and structural properties of each layer [9]. To the best of our knowledge, there is however no such thing in the literature as a detailed quantitative study of the interplay, as a function of depth, between strain and chemical composition in such complex (Si)GeSn stacks.

The objective of this study is therefore to acquire chemical and structural information at the nanometer scale, in order to derive information on the incorporation of chemical species in (Si)GeSn alloys. We notably search to better understand the strain evolution at interfaces between the various layers its impact on the incorporation of chemical species. In the first part, the growth of thick, optically active GeSn layers will be investigated by comparing a monolayer structure (composed of a single active layer grown at constant temperature), with a step-graded one. The second part will focus on the properties of thin SiGeSn layers used as confinement barriers below and above thick optically active GeSn layers. We will especially focus on the impact of the lattice parameter of the template underneath on the SiGeSn barriers' strain state and chemical composition. We will also discuss the consequences on the emission properties of the devices.

2. Experimental details

2.1. Growth conditions

The growth of Ge, GeSn and SiGeSn layers was performed in a 200 mm Epi Centura 5200 reduced pressure chemical vapor deposition (RP-CVD) cluster tool from Applied Materials, on nominal Si(001) substrates. Firstly, 2.5 µm thick Ge Strain-Relaxed Buffers (SRB) were grown to accommodate the lattice mismatch between (Si)GeSn and Si. Germane (GeH_4) diluted at 2% in H_2 was used as the germanium gaseous precursor. The Ge layers were grown using a low temperature / high temperature approach followed by a short duration thermal cycling to reduce the threading dislocations density, which was close to 10^7 cm^{-2}. Ge growth conditions are detailed elsewhere [18–20]. Samples were then kept at 20 Torr under ultra-pure N_2 in the load-locks of the tool to avoid surface oxidation. Afterwards, the wafers were loaded in the dedicated epitaxy chamber of the cluster tool equipped with low temperature infra-red pyrometers. The samples were annealed under H_2 at 800 °C for 2 minutes prior to low temperature GeSn and SiGeSn growth on top. The 100 Torr growth was performed using digermane (Ge_2H_6), tin tetrachloride ($SnCl_4$) and disilane (Si_2H_6) as gaseous precursor, and dihydrogen (H_2) as a carrier gas. Flows were kept constant, while the temperature was chosen to reach the targeted Si and Sn concentrations, as described in references [21–23]. Concentrations in those studies were calibrated on thin, pseudomorphic (Si)GeSn layers deposited on Ge SRB, in conditions identical to those in the current paper.

The impact of the device structure on the chemical and mechanical properties are studied thanks to three different samples. The first one, named CT349 (Constant Temperature) sample (**Figure 1b),** consists in a 450 nm thick GeSn layer grown at 313 °C with, nominally, a Sn concentration of 12% based on data on pseudomorphic layers. The second one, named SG (Step-

Graded) sample, is made of 5 layers with different Sn concentrations (**Figure 1c**). They were grown at 349 °C, 337 °C, 325 °C, 313 °C and 325 °C, resulting in nominal concentrations of 6%, 8%, 10%, 12% and 10%, respectively [23]. The highest concentration layer was grown over a longer period of time, in order to have a thick emissive layer. For both samples, the GeSn layer(s) were sandwiched between 20 nm thick SiGeSn layers grown at the same temperature of 349 °C. Those samples were used to better understand the impact of a step-graded structure on Sn incorporation and on the strain state of the GeSn emissive layer.

The same CT349 sample is also used to study the impact of starting lattice parameter on the growth of the thin SiGeSn layer. The comparison is made with a third sample called CT325 (**Figure**

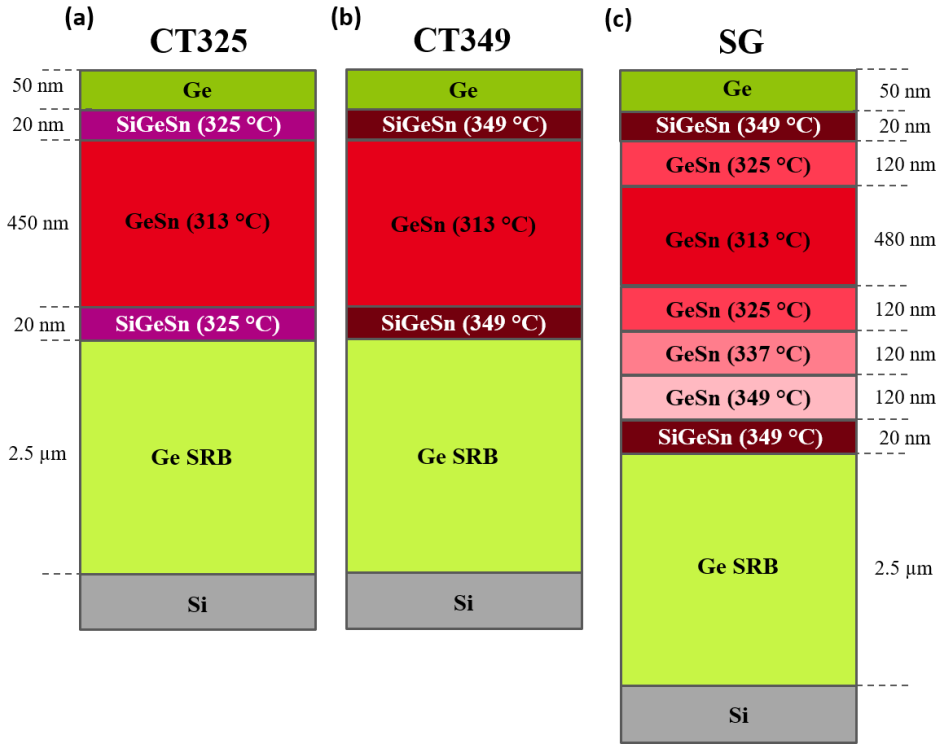

Figure 1. Schematics studied samples. (a) CT325 and (b) CT349 own a unique GeSn emissive layer grown at constant temperature, sandwiched between two SiGeSn confinement layers grown at (a) 325°C and (b) 349 °C, respectively. (c) Step-graded (SG) structure with five GeSn layers grown at different temperatures and two SiGeSn confinement barriers grown at 349 °C.

1a), whose GeSn structure was identical to that of the CT349 sample. The only difference was the growth temperature of the two SiGeSn confinement layers, grown at 325 °C instead of 349°C. As described in [22,23], these growth temperatures (325 °C and 349 °C) should result in, nominally, $Si_{0.054}Ge_{0.841}Sn_{0.105}$ layers for CT325, and $Si_{0.083}Ge_{0.839}Sn_{0.078}$ layers for CT349.

2.2. Material characterization

Samples were prepared for TEM by Ga+ Focused Ion Beam (FIB) using a standard lift-out technique, and deposited onto molybdenum or copper TEM grids. The SG sample was prepared using a FEI Helios 450 machine, while a FIB-SEM Zeiss Crossbeam 550 was used for the CT325 and CT349 samples. In order to prevent shadowing of the X-rays detectors from the grids, samples were placed on the front side of the finger, after the removal of part of their sidewalls.

TEM analyses were performed on a probe-corrected TFS Titan Themis microscope operating at 200 kV, equipped with a Super-X detector system for Energy-dispersive X-ray (EDX) spectroscopy. The system comprises four 30mm² windowless silicon drift detectors integrated into the pole piece with an elevation angle of 18°. Detectors are symmetrically placed around the beam axis at 45°, 135°, 225° and 315° azimuthal angles, enabling a collection efficiency of 5.1 ± 0.5% assuming a solid angle of 0.64 ± 0.06 sr [24]. Mechanical properties of the material were measured by two different techniques depending on the desired field of view, i.e. precession electron diffraction (PED) to cover the full GeSn stack and geometrical phase analysis (GPA) applied to STEM-HAADF images for the thin SiGeSn barriers. A detailed review article discussing the strengths and weaknesses of both techniques can be found in [25]. Precession Electron Diffraction (PED) was performed on CT and SG samples by acquiring the local diffraction patterns on a Gatan

US1000 CCD camera. This approach enabled us to measure quantitative strain maps with a spatial resolution of 10 nm, corresponding to the scan step used for this analysis [26]. In order to simultaneously acquire EDX spectra and diffraction patterns, a homemade Digital Micrograph (DM) script was developed. The later was used to synchronize the scanning beam and the detectors used for analysis, as detailed in [27]. Analyses of CT325 and CT349 samples were performed using GPA [28], by acquiring high-resolution HAADF images of the structures on 114 nm x 114 nm area and using a pixel size of 28 pm. In order to investigate both in-plane and out-of-plane lattice distortions of the SiGeSn layers and prevent artefacts due to beam scanning distortions, two acquisitions were performed on each zone, by rotating the scan direction by 90° [29]. Only the information parallel to the scan direction was kept for each acquisition.

2.3. Data analysis

The net intensities of the Ge-K and Sn-L X-ray lines were extracted from EDX spectra using the Kramer's background subtraction method and Gaussian deconvolution, as implemented in Gatan Microscopy Suite 3 (GMS 3). Such intensities were used to quantify the composition in the various layers thanks to the IZAC code [30] which is based on the ζ-factors approach [31], in order to correct X-ray absorption in the quantification procedure. Pure Ge and Sn references samples with known thicknesses were used in order to accurately calibrate ζ-factors.

Two data are required in order to characterize the mechanical properties of individual layers in such stacks: the intrinsic residual deformation ε and the crystal relaxation R compared to the Ge virtual substrate. They are given by the following equations:

$$\varepsilon^{\parallel}_{GeSn} = \frac{a^{\parallel}_{GeSn} - a^{0}_{GeSn}}{a^{0}_{GeSn}}, \qquad R^{\parallel}_{GeSn} = \frac{a^{\parallel}_{GeSn} - a^{\parallel}_{GeVS}}{a^{0}_{GeSn} - a^{\parallel}_{GeVS}} \tag{1}$$

$a^{\parallel}_{GeSn}$ being the in-plane lattice parameter of the GeSn layer, $a^{\parallel}_{GeVS}$ the in-plane lattice parameter of the Ge SRB or Virtual Substrate (VS), and a^{0}_{GeSn} the relaxed lattice parameter of the GeSn layer. The latter only depends on the chemical composition, and can be calculated by using a positive deviation from the Vegard's law:

$$a^{0}_{GeSn}(x_{Sn}) = x_{Sn}a^{0}_{Sn} + (1 - x_{Sn})a^{0}_{Ge} + x_{Sn}(1 - x_{Sn})\beta_{GeSn} \quad (2)$$

where $a^{0}_{Sn} = 6.489$ Å and $a^{0}_{Ge} = 5.65756$ Å are the lattice parameters of pure Sn and Ge crystals, respectively. $\beta_{GeSn} = 0.041$ Å is the bowing parameter and x_{Sn} the atomic fraction of Sn in the alloy, given by EDX measurements [32].

PED and GPA analyses measure the relative deformation $e^{\parallel}_{GeSn}$ compared to the substrate lattice parameter (i.e. Lagrangian definition):

$$e^{\parallel}_{GeSn} = \frac{a^{\parallel}_{GeSn} - a^{\parallel}_{GeVS}}{a^{\parallel}_{GeVS}} \quad (3)$$

Note that this analysis supposes that the lattice parameter $a^{\parallel}_{GeVS}$ of the Ge VS is known in order to compute ε and R. In the case of the Ge virtual substrate, it has been shown by XRD analyses that the crystal is slightly tensile strained ($103\% < R^{\parallel}_{GeVS} < 104\%$). This is due to thermal expansion coefficient differences between Si and Ge coming into play when cooling down to room temperature [18,22,32].

By combining the previous equations, we obtain:

$$\varepsilon^{\parallel}_{GeSn} = \left(e^{\parallel}_{GeSn} + 1\right)\frac{a^{\parallel}_{GeVS}}{a^{0}_{GeSn}} - 1\,, \qquad R^{\parallel}_{GeSn} = \frac{e^{\parallel}_{GeSn}\, a^{\parallel}_{GeVS}}{a^{0}_{GeSn} - a^{\parallel}_{GeVS}} \quad (4)$$

Finally, in order to increase the accuracy of EDX and PED measurements and better analyze their evolution along the growth direction, the experimental Sn concentration x_{Sn} and relative deformation e_{GeSn} maps were projected along the in-plane direction.

3. Sn incorporation into GeSn

The emissive properties of GeSn is strongly dependent on its composition and on the crystal strain. Alloys with high amounts of Sn and plastically deformed, low residual compressive strain crystalline structures are generally targeted. The evolution of these properties with respect to growth temperature, precursor gas flows or layers thicknesses was investigated in the literature [21,33]. As analyses were mainly performed using non-local techniques such as XRD/RSM or WDXRF, discrete contributions of layers with compositions which were close, inhomogeneous and with interface effects could not be probed. They can, however, play an important role in the growth of a structure and determine the light emission properties of devices. The aim of this section is to bring new insights into the properties of GeSn emissive layers, notably by studying the impact of device structures on crystalline properties. To that end, EDX and PED in the STEM were performed on CT349 and SG samples. For the sake of convenience, the CT349 will simply be referred to as the CT sample in this section.

3.1. Results

Results from PED-EDX analysis of the SG sample are shown as examples in **Erreur ! Source du renvoi introuvable.**. A virtual reconstruction of the ADF signal is shown in **Erreur ! Source du renvoi introuvable.a**, by integrating the intensity recorded around the direct beam on the camera. It helps to reveal the overall structure of the different layers in the sample, as well as the dislocation network formed during growth. **Erreur ! Source du renvoi introuvable.b-c** show the quantitative chemical maps obtained from the EDX analysis of Sn and Ge, respectively. We easily identify the five GeSn layers grown at different temperatures (**Figure 1c**). **Erreur ! Source du renvoi introuvable.d** and **e** give the relative deformation *e* in the growth plane and along the

growth direction, respectively. The relative in-plane deformation is between 0.0 and 2.0%. It is at its highest in the two top layers. This indicates that there was some partial relaxation during growth, as the in-plane lattice parameter of these layers was definitely higher than that of the Ge VS underneath. The out-of-plane lattice parameter has also significantly increased compared to that of the Ge VS, up to 3% in the 4th layer. More insight about crystal deformation will be obtained by computing the strain and relaxation, as described in section 2.3. Finally, **Erreur ! Source du renvoi introuvable.f-g** depict the local shearing and rotation of the GeSn crystal, respectively. As explained in [34], strong rotation variations between negative and positive values, as seen in **Erreur ! Source du renvoi introuvable.g**, are typical of the presence of dislocations. Hence, one can notice the strong concentration of such dislocations at the interfaces of the first three layers, as

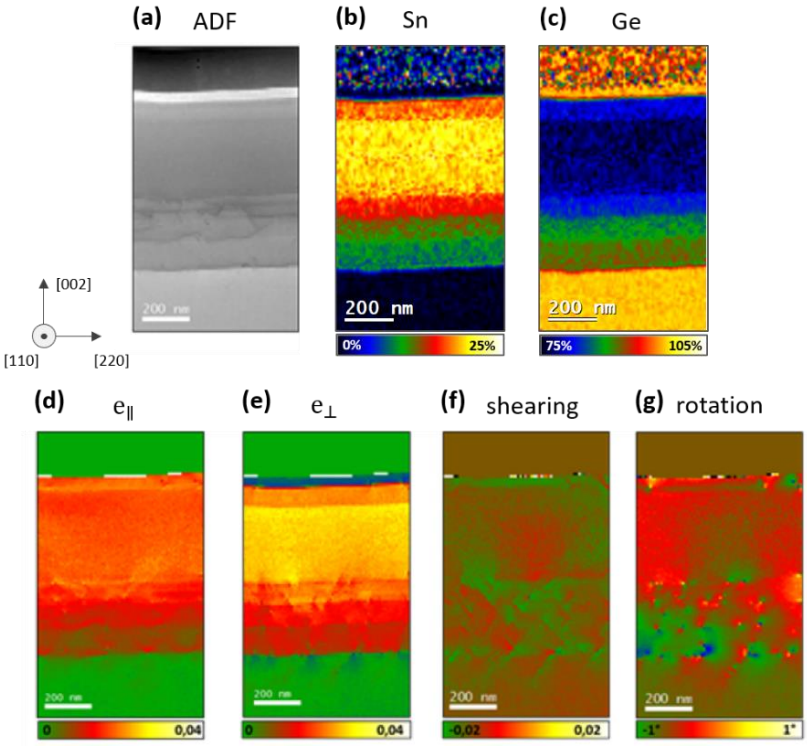

Figure 2. Correlative PED-EDX analysis of the SG sample. (a) Virtual ADF image, (b-c) Sn and Ge concentration maps obtained from EDX, (d-e) in-plane and out-of-plane deformation, (d) shearing and (e) rotation of crystalline plans.

confirmed by the virtual ADF image and shearing map (**Erreur ! Source du renvoi introuvable.a** and **f**). Conversely, no noticeable presence of dislocations are visible in the two last layers, including the thickest GeSn emissive layer.

In order to quantitatively study the mechanical properties of the CT and SG samples, and correlate them with chemical evolution in the two structures, we calculated the deformation ε and the relaxation R from EDX and PED analysis results thanks to equations (4) (section 2.3). Additionally, rotation maps presented in **Erreur ! Source du renvoi introuvable.e** were filtered and normalized to compare the two samples in terms of relative dislocation density ρ_d through the layers. More details about this procedure can be found in **Appendix A**. To increase the statistics from EDX and to give a realistic representation of the layers from PED, all the experimental data were projected along the growth plane direction before calculating ε and R, resulting in a line profile evolution through the layers. Results are shown in **Figure 3**.

Figure 3a-c show results for the CT sample. The EDX Sn concentration profile (black curve) reveals a non-uniform chemical distribution in the emissive layer. Indeed, the chemical profile shows the presence, at the bottom, of a first layer (I) with a first strong Sn concentration increase up to 11.5 at.%, followed by a quasi-constant chemical composition which slightly increased up to 12.4 at.%. These values are perfectly in line with the nominal Sn concentration expected from data on pseudomorphic layers. This first layer has a thickness of around 180 nm. This is followed by a strong Sn incorporation (II), with a long increase of the Sn concentration up to 14.8 at.%. Note that, as the temperature was not changed during the growth of this layer, this sudden change of Sn incorporation is a spontaneous mechanism happening during growth. In layer I, the GeSn crystal is slightly compressed in the growth plane, with both a constant deformation of about -0.3% and a relaxation approximately equal to 83%. When the crystal begins to incorporate

more Sn in layer II up to 15 at.%, the in-plane lattice becomes more strained, reaching a value of -0.87% at the top of layer II. The relaxation therefore drops from more than 80% at the bottom down to 60% at the top of layer II. **Figure 3c** plots the relative density ρ_d as a function of depth, showing that defects are mostly present at the Ge VS/GeSn I and GeSn II/Ge interfaces. Some are also present, to a lesser extent, inside layer I. When layer II began to grow, no traces of dislocations could be detected.

Figure 3d-f depicts the less intuitive behavior of mechanical properties in the SG sample, due to the different structure of the device. The EDX analysis shows that all GeSn layers exhibit at first a gradual Sn concentration increase followed by a region over which the chemical composition remains almost constant, before the next layer and thus the next growth temperature change. Sn concentrations in the five layers were of 7.1 at.%, 9.5 at.%, 12.4 at.%, 15.8 at.% and 13.5 at.%, respectively. The values measured are relatively far from the nominal values targeted (6%, 8%, 10%, 12% and 10%), especially in layers away from the Ge SRB. In the first three layers (I, II and III), the crystal is slightly in compression in the growth plane, with a strain reduction before each interface. This behavior can also be found in the relaxation curve which shows the same periodic pattern, confirming that the crystal tends to fully relax at each interface. Note that at positions closer to the emissive layer (IV), the crystal seems to be less and less deformed and is almost completely relaxed, even at the center of layers. In parallel, **Figure 3f** plot of the relative density ρ_d as a

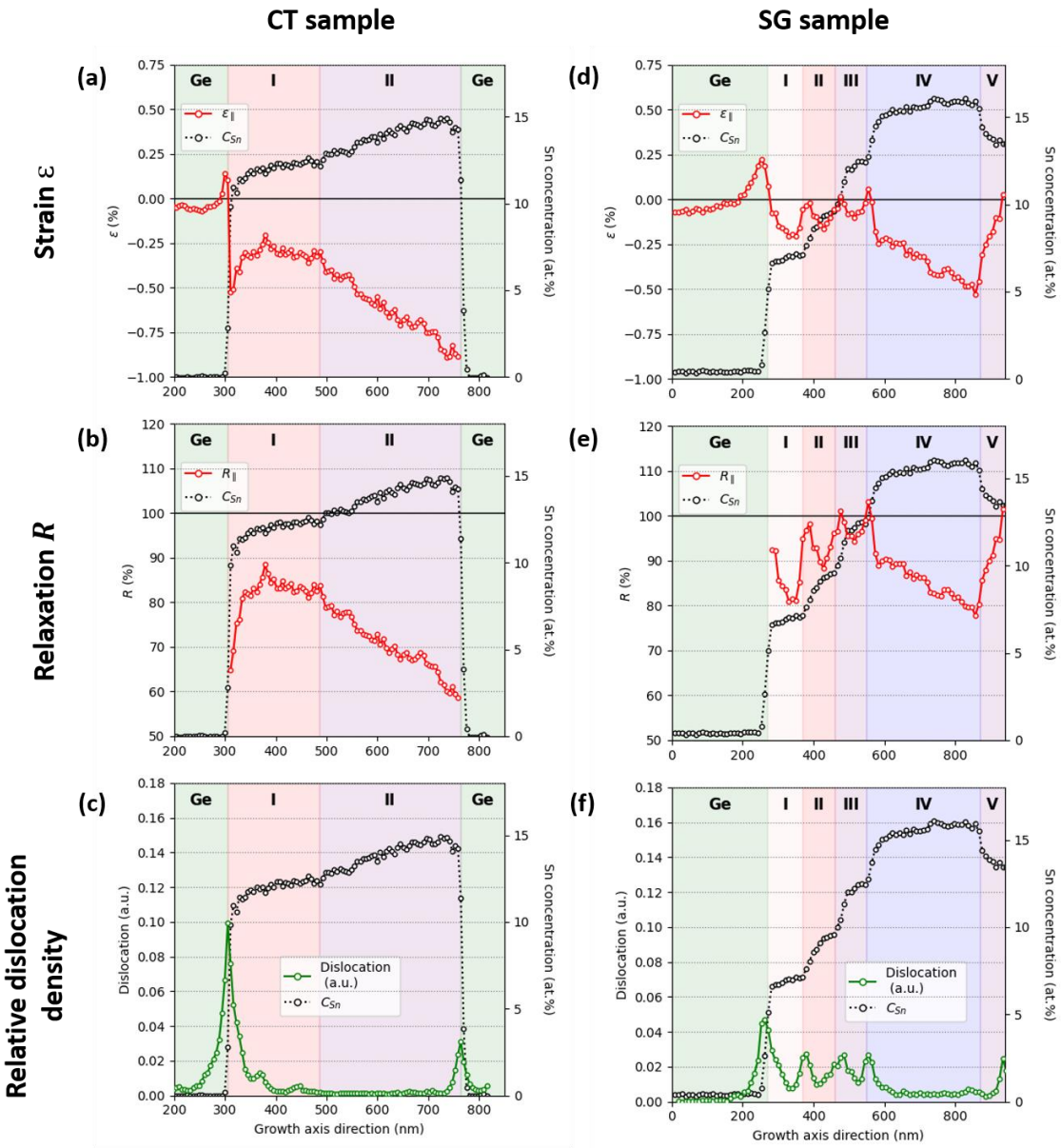

Figure 3. Evolution of deformation ε, relaxation *R* coefficients calculated from equation (4), and relative dislocation density distribution for monolayer (a-c) and step-graded (d-f) samples, respectively.

function of depth shows that defects are much more present, with lesser densities, at the interfaces between GeSn layers I, II and III, compared to the monolayer, e.g. the CT sample. The strain state

observed with PED in the two structures are completely in line with RSM measurements realized by Aubin *et al.* [9] on structures that were very close.

3.2. Discussions

Figure 3a shows a strong Sn concentration increase, from ~ 12.5 up to ~ 15 at.%, for the CT sample deposited at a constant temperature of 313°C. This spontaneous Sn content increase in thick CVD-grown GeSn layers was reported before in the literature [9–11,15,17]. It was attributed to strain evolution upon growth in such layers. By using a Gibbs free energy theoretical analysis, Dou *et al.* [10] made the demonstration that a relaxed GeSn layer was prone to incorporate a higher amount of Sn compared to a compressive strained crystal. These predictions were confirmed by monitoring the relaxation state of GeSn layers, mostly thanks to XRD, for different growth thicknesses [9–11,15,17,35]. These studies were performed on numerous samples grown with a wide range of parameters providing statistically relevant data on the impact of the mechanical state on Sn incorporation.

Note that our PED results do not actually represent the strain evolution occurring during the growth due to potential mechanical relaxation either imposed after the full stack deposition or generated during cooling (related to differences in thermal expansion coefficients). However, we will strive here to better understand the Sn incorporation mechanism by correlating the local strain state with the Sn composition profile and by comparing results with literature data on various thicknesses GeSn layers. Thus, it was shown [15] that the plastic relaxation of the strong compressive strain in such layers happened in two stages with different critical thicknesses. A first one (h_G) concerns the nucleation and the gliding of misfit dislocations at the GeSn/Ge-VS interface, while the second one (h_N) marks the start of the interaction and multiplication of the dislocation network. The spontaneous Sn enrichment on CT sample occurs for a deposition thickness h_N of ~

190 nm, in line with a h_N of 170 nm ± 20 nm measured by Assali *et al.* [11] for a Sn content of ~ 15.5 at.%. Hence, this 190 nm thick critical layer corresponds to the thickness needed by the material to be partially relaxed after plastic deformation, as shown from the relaxation curve in **Figure 3c**. As shown in **Figure 3a-b**, the GeSn layer then begins to compress in the growth plane when Sn incorporation starts to increase within layer II. It results in in-plane strain and relaxation drops to negative values. This explains why, after a Sn enrichment over more than 200 nm, the composition saturates as the crystal is then in a much more compressive configuration.

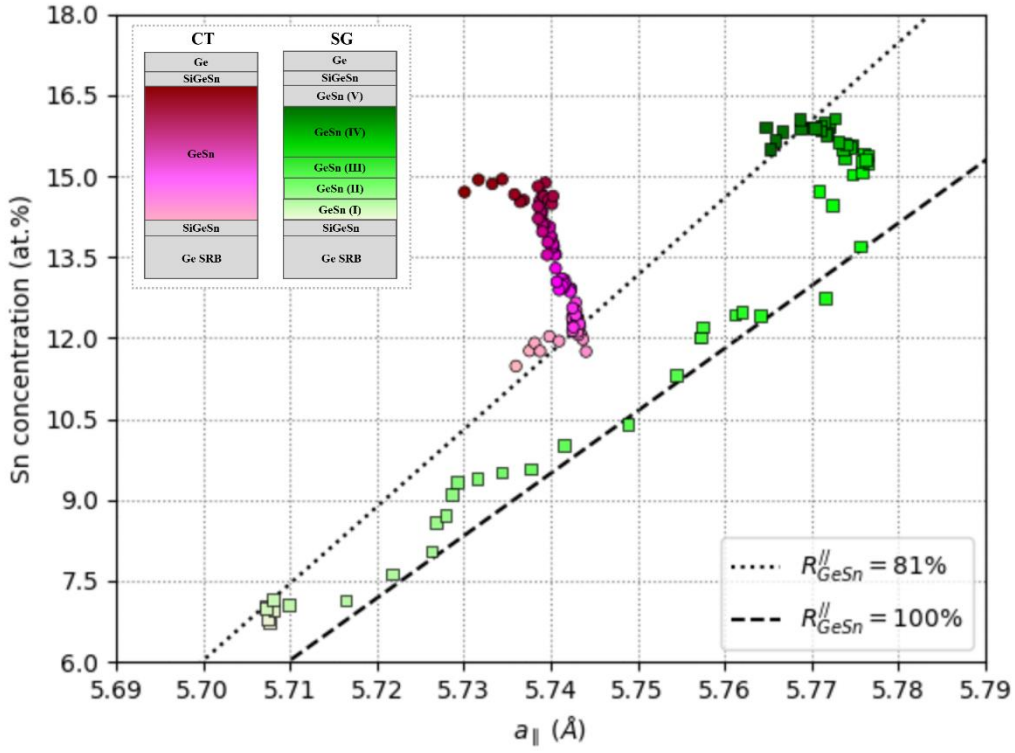

Figure 4. Correlation between Sn concentration and the in-plane ($a_{\parallel}$) lattice parameter for CT and SG samples. Color gradients (from bright to dark) illustrate the position, from bottom to top, in the heterostructures. The dotted and dashed lines indicated the linear relationship between the Sn concentration and $a_{\parallel}$ for crystals with 81% and 100% of relaxation, respectively. For clarity, the last (V) layer of SG sample was not included in the profile, as it imposed a reduction of Sn content in the layer.

As it is not possible from XRD analyses to follow the local strain evolution through the material, we propose here a more direct evidence of the interplay between strain and chemical composition. To that end, the Sn composition is plotted in **Figure 4** as a function of the in-plane ($a_{\parallel}$) GeSn lattice parameter for the two structures. Two lines are plotted on the graph to localize zones where the crystal is relaxed at 81% and 100%, respectively. For the CT sample, we can identify three different regimes. The Sn concentration, which is mainly governed by the growth temperature (313°C), directly starts at ~11.5 at.% and quickly stabilizes around 12 at.% with a lattice parameter of 5.745 Å, then, corresponding to the 81% relaxation identified in layer I (**Figure 3b)**. In this zone, the crystal almost remains unchanged until it starts to incorporate more Sn in layer II, with then a slight decrease of the in-plane lattice parameter down to 5.74 Å. A third behavior is observed at the top of the GeSn emissive layer, with a strong reduction of $a_{\parallel}$ down to 5.73 Å at constant Sn concentration. As the growth of the first layers of the SG sample occurred at higher temperatures, both the Sn concentration and the in-plane lattice parameter were lower in those. Interestingly, the first layer relaxation is also around 80%, just as the bottom part of the CT sample. But, thanks to the different growth temperatures used, we clearly observe oscillations of the in-plane lattice parameter around the 100% relaxation line, this up to the highly concentrated GeSn layer IV grown at 313 °C. Indeed, the $\varepsilon_{\parallel}$ and $R_{\parallel}$ profiles in **Figure 3.d-e** have U-shapes within each of the first three layers of the SG sample. This indicates that, before the growth of the next layer, the crystalline layer underneath is completely relaxed, due to the formation of misfit dislocations at the interfaces between those layers as revealed in **Figure 3f**. The three Sn concentration steps used in the SG sample are enough to obtain an almost completely relaxed layer III ($R_{\parallel} > 95\%$ in the entire layer). Compared to sample CT, we clearly see that starting from a small lattice parameter enabled to reach much higher $a_{\parallel}$ values up to 5.775 Å. As a consequence,

the layer grown at 313°C (i.e. the same temperature growth than CT sample emissive layer) directly reached a Sn composition of 15 at.%. As for layer II in the CT sample, layer IV then starts to spontaneously enrich in Sn up to a concentration of 16 at.% with a slight reduction of the lattice parameter. Finally, we also observed a strong reduction of lattice parameter at constant Sn content.

Even though the Sn content difference between the two emissive layers is less than 1 at.%, we observe a significant increase by 0.03 Å of the in-plane lattice parameter in the SG sample compared to the CT one. This demonstrates the advantage of having a gradual decrease of the growth temperature in order to fully relax the structure at some stages during the growth. This approach yields a highly relaxed, defect-free emissive layer, which is necessary for optimum emission properties. Note that the in-plane lattice parameter of the emissive layer spontaneously decreases with thickness at the final stages of growth. This indicates that increasing the thickness of these layers can potentially deteriorate the emission properties, as the Sn concentration stays constant while some compressive strain builds up (less direct bandgap).

As a final comment, **Figure 3c** shows that a large portion of dislocations in the CT sample is formed at the interface between the Ge buffer and layer I, i.e. in a material with almost 12 at.% of Sn. The presence of a defective GeSn alloy with such a strong Sn concentration next to the emissive layer might result in non-radiative recombination, which can considerably lower the emission efficiency of the overall structure [36,37]. Meanwhile, the step-graded structure keeps most of the defaults located in lower Sn concentration layers away from the emissive layer (**Figure 3f**). The amount of defects in layers III and IV (i.e. where non-radiative recombination could take place) is comparatively low, helping in maintaining a good emission efficiency of the overall stack. No defects in the emissive layers of both samples are detected by PED analysis, neither threading

dislocations from the virtual ADF image or shear maps, nor misfit dislocations from the rotation maps.

In summary, the analysis of the CT sample shows how a GeSn crystal grown at a constant temperature is spontaneously enriched in Sn as soon as a critical thickness is reached. A deposited thickness of 190 nm at a constant 313°C temperature on a Ge buffer provides a fully relaxed GeSn layer with a Sn content of ~ 12 at.%, which is the condition to initiate a spontaneous in-plane lattice expansion resulting in a gradual Sn incorporation. Another approach is to gradually lower the growth temperature, in order to create intermediate layers to progressively accommodate the lattice parameter mismatch, as in the SG sample [9–11]. A similar fully relaxed $Ge_{0.88}Sn_{0.12}$ structure is obtained after the deposition of three intermediate layers at 349 °C, 337 °C and 325 °C. In the layer grown on top at 313°C, there is a rapid Sn incorporation increase and some lattice expansion. But unlike the sample grown at constant temperature, this progressive lattice adaptation provides (i) a highly relaxed GeSn crystal and (ii) the creation of misfit dislocations far from the emission layers (reducing non-radiative recombination), which are two criteria beneficial for the emission properties.

4. Si and Sn incorporation in SiGeSn confinement barriers

SiGeSn barriers exhibit a significant larger bandgap than GeSn and can efficiently confine charge carriers into emissive layers [22,38]. This property is highly influenced by the material composition and mechanical state [39]. In order to benefit from high quality SiGeSn confinement barriers, such layers should be pseudomorphic on the Ge SRB or the GeSn stack underneath, explaining why their thicknesses should not exceed a few tens of nm, typically.

The purpose of this section is to understand how the lattice parameter of the template will impact, for a given set of process parameters, the composition of SiGeSn crystals. In order to characterize both chemical and mechanical properties of such ternary alloys, EDX and GPA analyses were performed on CT325 and CT349 samples (**Figure 1a** and **b**). Due to their relative small dimensions (compare to the GeSn layer), GPA is a more appropriate technique to study the SiGeSn lattice parameters evolution compared to that of layers underneath [28]. As a reminder, there was in each sample two SiGeSn layers grown at the same temperature (325°C or 349°C) encapsulating a single thick GeSn layer identical to that in the CT sample. Those layers will be called, in the following, bottom and top layers, referring to their respective positions in the heterostructure.

4.1. Results

Figure 5 gathers results obtained on top and bottom SiGeSn layers thanks to GPA analysis on CT325 and CT349 samples. The HAADF signal recorded for the analysis is shown in the left column, followed by the in-plane and out-plane relative displacements e from GPA analysis (middle and right column). There are strong mechanical behavior differences between SiGeSn top

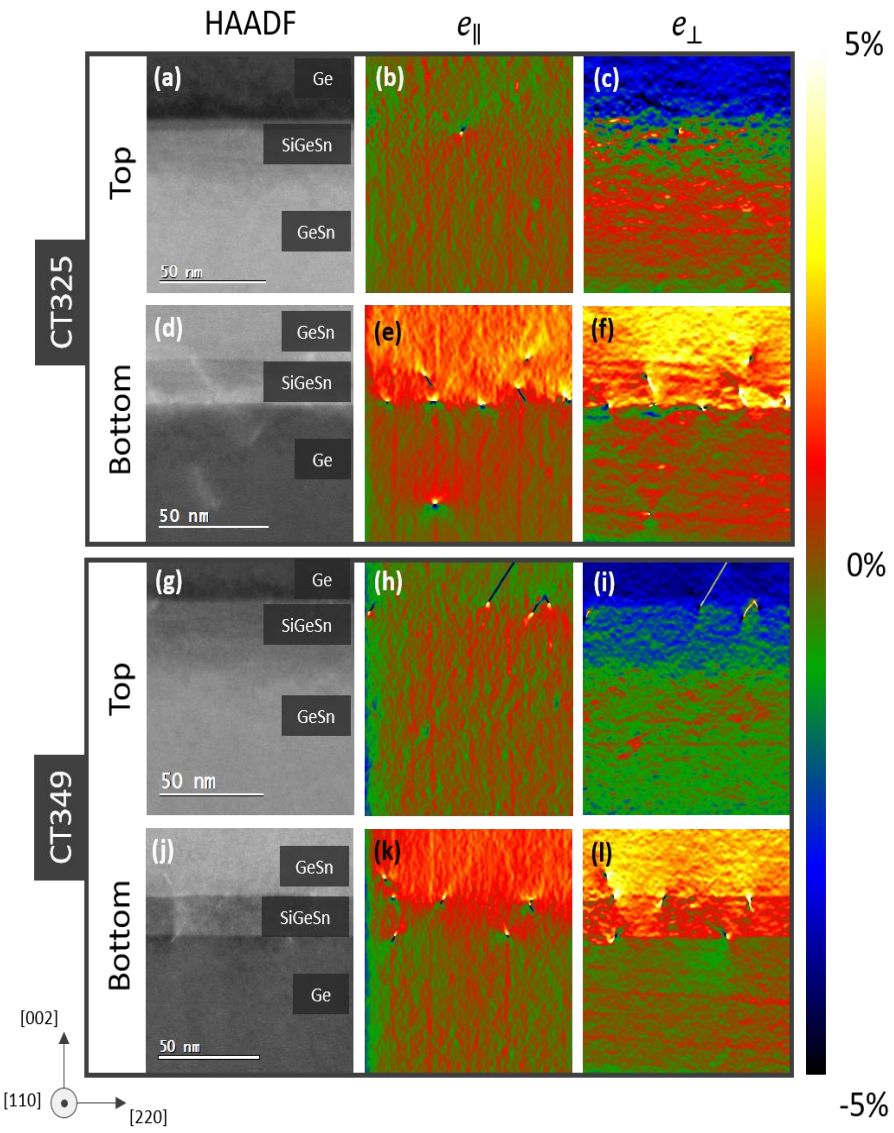

Figure 5. Lattice distortion analysis by GPA of the bottom and top SiGeSn confinement barriers in samples CT325 (a-f) and CT349 (g-l). Left column: HAADF image used for the analysis. Middle and right columns: in-plane ($e_{\parallel}$) and out-of-plane ($e_{\perp}$) lattice mismatch measurement.

and bottom layers. **Figure 5d** shows the HAADF image of CT325 sample's SiGeSn bottom layer between the Ge SRB and the emissive GeSn layer. The in-plane lattice parameter substantially increases, with a relative difference up to 2%, when switching over from the Ge virtual substrate

to the confinement barrier, as shown in **Figure 5e**. This means that the layer is partially relaxed. However, by comparing **Figure 5e** and **f**, one can note that the out-of-plane lattice parameter has increased even more, reaching values of almost 3%. This difference between in-plane and out-of-plane lattices indicates that the crystal is not fully relaxed. Conversely, no noticeable change of in-plane lattice parameter is observable between SiGeSn and the bottom part of the emissive GeSn layer, indicating a good lattice match. This GeSn crystal is subjected to a compressive strain in the growth plane, which is compensated by a tensile strain in the out-of-plane direction. This Poisson effect is visible in **Figure 5f,** with lattice distortion of around 4% compared to the Ge buffer. Note that, the GPA analysis being based on the measurement of local displacements of atomic columns detectable at high resolution, strain maps are also sensitive to crystal distortions because of dislocation stress fields [40,41]. This explains why it is feasible to visualize those dislocations, mostly located at the Ge/bottom SiGeSn interface (**Figure 5e-f**).

The situation is considerably different for the top layer of the same sample, as shown in **Figure 5a-c**. There is a very poor HAADF signal contrast between the upper part of the emissive GeSn layer and the confinement barrier. No change of the in-plane lattice parameter is measurable, showing that the SiGeSn confinement barrier and the Ge capping were fully pseudomorphic on the emissive GeSn layer underneath. As these materials have a different relaxed lattice parameter (depending on their chemical concentrations), it results in a lattice distortion along the growth direction of about -1% for SiGeSn and up to -3% for the Ge capping. Note that only one dislocation located at the SiGeSn/Ge interface was detected by GPA.

Results for the CT349 sample (**Figure 5g-l**) are pretty close to that for the CR325 sample. **Figure 5k** indicates a more gradual increase of the in-plane lattice parameter when switching from the Ge SRB to the bottom SiGeSn layer, reaching relative deformation values of about 1.5%. Yet

again, the material is more distorted along the growing direction (**Figure 5l**), with a definite boundary between the confinement barrier and the bottom part of the GeSn emissive layer. Dislocations are located at the interfaces between the three layers, as shown by the deformation maps. Despite a growth temperature difference, the top SiGeSn layer in sample CT349 behaves similarly to that in sample CT325, as shown in **Figure 5g-i**. The barrier is fully pseudomorphic on the upper part of the GeSn emissive layer, resulting in a reduction of the lattice parameter along the growth direction in the barrier and the Ge capping. A few dislocations are also visible in this Ge cap.

EDX profiles of the chemical concentration in those SiGeSn layers are shown in **Figure 6**. As a reminder, top and bottom confinement barriers were grown with the same temperature, pressure and precursor flows in each sample, i.e. the very same compositions were targeted. There is a superposition in each graph of results obtained on the two different SiGeSn layers for each sample, enabling a direct composition comparison between them. In **Figure 6a**, profiles with empty round markers show the evolution of Si (red) and Sn (blue) composition though the Ge/SiGeSn/GeSn layers, i.e. in the bottom part of the stack of sample CT325. The mean chemical composition of this confinement barrier, with 5.7 at.% of Si and 10.5 at.% of Sn, is in excellent agreement with that in the pseudomorphic $Si_{0.054}Ge_{0.841}Sn_{0.105}$ layer obtained, with the same growth conditions, in references [22,23]. The GeSn layer on top has a Sn concentration of 12.1 at.%, similar to that in the monolayer CT sample (**Figure 3**). Chemical composition differences in the top layer are obvious when looking at the filled triangles in the same figure. While this layer is grown at the same temperature, pressure and the very same flows, the Sn concentration is 14.0 instead of 12.1 at.%. Meanwhile, the Si concentration slightly drops from 5.7 down to 4.6 at.%.

The upper part of the GeSn emissive layer is visible on the left part of the graph, with a mean Sn concentration of 15.1 at.%, in line with that in the CT sample.

Figure 6b show profiles in the two confinement barriers of CT349 sample. As before, there is an excellent agreement between targeted and measured concentrations for the bottom barrier. We indeed had 8.1 at.% of Si and 7.9 at.% of Sn, in line with that in the pseudomorphic $Si_{0.083}Ge_{0.839}Sn_{0.078}$ layer obtained, with those growth conditions, in references [22,23]. The concentration of Sn increased in the bottom part of the emissive layer, reaching 11.6 at.% of Sn, i.e. a value slightly lower than that in the CT325 sample. The very same chemical modifications are observed for the top SiGeSn layer, with a Sn enrichment (10.6 instead of 7.9 at.%) and a slight Si depletion (7.2 instead of 8.1 at.%). There is otherwise a significant drop of the Sn content (from

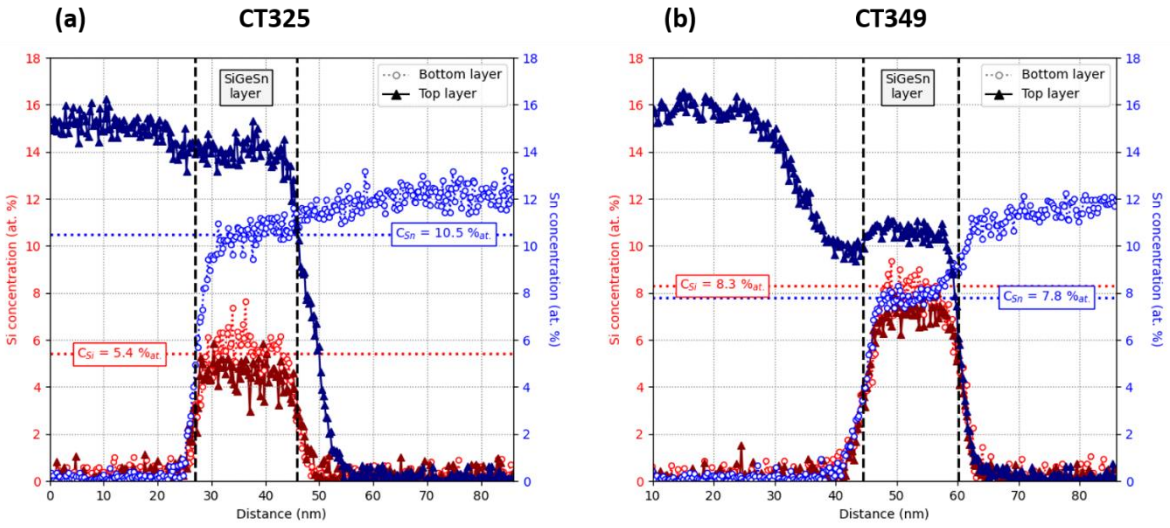

Figure 6. Si and Sn concentrations profiles along the growth direction from EDX for (a) the CT325 sample and (b) the CT349 sample. Profiles for the bottom layer (empty round markers) and top layer (filled triangle markers) are superimposed on both figures. As reference, the horizontal colored dashed lines represent the nominal concentrations targeted during the growth.

16.0 down to 10.0 at.%) in the upper 20 nm of the GeSn emissive layer just below the SiGeSn top barrier. It is due to the fact that we had to move from 313°C (the growth temperature of the emissive layer) up to 349°C (the growth temperature of the SiGeSn top barrier) while still flowing Ge_2H_6 and $SnCl_4$ inside the growth chamber to inhibit Sn droplet formation on the surface. This resulting in the Sn concentration grading that can be seen in **Figure 6b**.

4.2. Discussion

The previous section has highlighted the strong differences between the top and bottom SiGeSn layers for CT325 and CT349 samples. While the top barrier was pseudomorphically grown on the partially relaxed, high Sn content GeSn emissive layer with very few defects generated, compressive strain was partially relaxed in the bottom one through creation of misfit dislocations at Ge/SiGeSn and SiGeSn/GeSn interfaces (**Figure 5**). In parallel, **Figure 6** pointed out the modification of chemical concentration that occurred when growing the confinement barrier at different places in the heterostructure, this for the very same process parameters (temperature, flows, or pressure).

The major difference between the top and bottom layers in both samples is the starting lattice parameter (SLP) prior to epitaxial growth. For the bottom layer, the determination of the SLP is straightforward, as it only depends on the mechanical state of the Ge SRB, which is accurately known thanks to XRD measurements [18,22,32]. Conversely, the top layer SLP depends on the composition and the residual strain in the top part of GeSn emissive layer. EDX and PED results in section 3.1, used to compute the strain in the crystal (**Figure 3a**), can be used to determine

the SiGeSn top layer SLP. For the two samples, the SLPs for the bottom and top layers are 5.67 Å and 5.73 Å, respectively, i.e. a relative lattice parameter difference between 1.0 and 1.1%.

The consequence of this SLP modification is shown in **Figure 7**. For Si and Sn elements, the concentration differences with the nominal values (in pseudomorphic layers grown directly on Ge SRBs) are plotted for CT325 and CT349 samples, this as functions of the SLP. There is a significant influence of the SLP on the incorporation of both elements. While the bottom layers values exhibit a maximum deviation of 5% for Si in the CT325 sample and even less for Sn, top layers have lost around 14% of their Si content and increased their Sn content by up to 34%, approximately. The agreement between nominal and measured chemical content in the bottom layer was expected as the nominal concentrations were calibrated using single thin SiGeSn layers grown on the same type of Ge SRB. These results show the excellent EDX accuracy for the

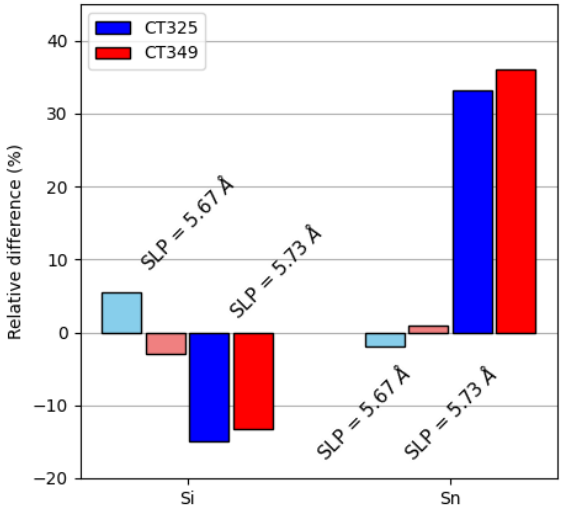

Figure 7. SiGeSn relative concentration differences compared to nominal values, depending on the starting lattice parameter of the layer. Comparison between CT325 sample (blue) and CT349 sample (red). The bright bars consider the results of the bottom layers, while the darkest bars concerns the top layers.

measurements of compositions of such ternary alloys, even in small scale heterostructures. Deviations measured for the top layers in the two samples are very close, and below the range of uncertainty of the bottom layers. This would indicate that the relative difference of composition in the confinement barriers depends much more on the SLP than on the deposition temperature. Therefore, the chemical concentration of such layer could be predicted with (i) an accurate nominal concentration calibration in well-established conditions (i.e. a good knowledge of substrate properties and growth temperature) and (ii) the precise knowledge of SLP at the particular position in the heterostructure where the SiGeSn layer must be grown.

Chemical composition and mechanical state changes are decisive for the capability of such alloys to play their roles as confinement barrier. A k·p model simulation developed for GeSn alloys [42] was adapted to SiGeSn alloys in order to simulate the variation of SiGeSn bandgap for the two confinement layers of each sample. Both chemical and mechanical information obtained from GPA-EDX analysis were included into the simulation. The results are summarized in **Table 1**. The energy separation between the Γ- and L-valleys enables to determine the material bandgap type. As we could expect, the SiGeSn bandgaps are higher for the CT349 sample compared to CT325,

Sample	**Layer**	**Γ gap (meV)**	**L gap (meV)**	**Γ/ L gaps difference (meV)**	**Gap type**
CT325	Bottom	592	584	8	Indirect
	Top	498	539	-41	Direct
CT349	Bottom	802	634	168	Indirect
	Top	567	570	-3	Direct

Table 1. k·p model simulation of SiGeSn energy bandgaps for the 4 confinement layers

the former having (in general) a higher content of Si and a lower content of Sn. For both samples, the bottom layer has a larger bandgap at Γ-point than at L-point, resulting in an indirect bandgap. Note that the difference in the case of CT325 sample is quite low. The situation is the opposite in the top layers, where the change of starting lattice parameter for the SiGeSn layer makes the bandgap slightly direct. This modification can drastically change the capacity of the structure to confine charge carriers into the emissive layer. However, the band-alignment between GeSn and SiGeSn is currently under investigation the exact band alignment GeSn/SiGeSn heterojunctions is not yet known [43].

5. Conclusion

STEM analyses were performed on (Si)GeSn heterostructures used as optoelectronic devices for mid infra-red light emission and which are CMOS compatible. Our aim was to correlate chemical and mechanical information, in order to better understand how the device stack can influence the properties of the different layers studied.

By combining quantitative, local EDX and PED analyses, the well-known spontaneous Sn enrichment in a thick GeSn layer deposited at a constant temperature of 313°C and therefore a nominal Sn content of 12% was clearly revealed. We showed that the thickness at which the material tended to partially relax after plastic deformation corresponded to the onset of more Sn incorporation, until a concentration of ~15 at.% was reached. The comparison was made with a strep-graded structure, with different layers grown at decreasing temperature. We showed that these layers progressively relaxed the strain, with two major benefits compared to a constant temperature structure:

- A significantly higher level of mechanical relaxation within the emissive layer
- The confinement of misfit dislocations at the bottom of the structure, reducing non-radiative recombination.

Hence, results indicated the beneficial impact of using a step-graded approach, instead of targeting a single thick GeSn layer grown at constant temperature.

Bottom and top 20 nm-thick SiGeSn confinement barriers were then studied to understand the impact of the in-plane lattice parameter of the template underneath (called the starting lattice parameter - SLP) on strain, Si and Sn content. For the two different samples studied (with different growth temperature for the barriers), we were able to show the influence of the mechanical state

on the incorporation of the Si and Sn into the structure by performing GPA and EDX. The higher the SLP was, the higher the Sn content and the lower the Si content were for a given set of process parameters. It seemed that the relative modification of chemical concentrations could be anticipated by knowing (i) the concentration of a layer grown in specific conditions (temperature, flows, pressure) on a given substrate (e.g Ge buffer) and (ii) the SLP difference when growing the layer on another crystalline template. By performing simulations, we showed how the bandgap of the SiGeSn layers to confine charge carriers was impacted by these chemical and structural modifications.

Our work showed that a better understanding of SiGeSn and GeSn key parameters (such as Sn content concentration and strain profiles) in complex light emission stacks can be obtained at the nanometer scale with STEM. It should help in optimizing future growths (threading dislocations and point defect management) and better quantify band alignments at Ge/(Si)GeSn hetero-interfaces, facilitating the design and fabrication of optimized type-I heterostructures.

6. References

[1] S. Wirths, D. Buca, S. Mantl, Si–Ge–Sn alloys: From growth to applications, Progress in Crystal Growth and Characterization of Materials. 62 (2016) 1–39. https://doi.org/10.1016/j.pcrysgrow.2015.11.001.

[2] A. Elbaz, D. Buca, N. von den Driesch, K. Pantzas, G. Patriarche, N. Zerounian, E. Herth, X. Checoury, S. Sauvage, I. Sagnes, A. Foti, R. Ossikovski, J.-M. Hartmann, F. Boeuf, Z. Ikonic, P. Boucaud, D. Grützmacher, M. El Kurdi, Ultra-low-threshold continuous-wave and pulsed lasing in tensile-strained GeSn alloys, Nat. Photonics. 14 (2020) 375–382. https://doi.org/10.1038/s41566-020-0601-5.

[3] B. Wang, E. Sakat, E. Herth, M. Gromovyi, A. Bjelajac, J. Chaste, G. Patriarche, P. Boucaud, F. Boeuf, N. Pauc, V. Calvo, J. Chrétien, M. Frauenrath, A. Chelnokov, V. Reboud, J.-M. Hartmann, M. El Kurdi, GeSnOI mid-infrared laser technology, Light Sci Appl. 10 (2021) 232. https://doi.org/10.1038/s41377-021-00675-7.

[4] K.P. Homewood, M.A. Lourenço, The rise of the GeSn laser, Nature Photon. 9 (2015) 78–79. https://doi.org/10.1038/nphoton.2015.1.

[5] J. Mathews, Z. Li, Y. Zhao, J. Gallagher, I. Agha, J. Menendez, J. Kouvetakis, Toward GeSn Lasers: Light Amplification and Stimulated Emission in GeSn Waveguides at Room Temperature, ECS Trans. 75 (2016) 163–176. https://doi.org/10.1149/07508.0163ecst.

[6] Z.-M. Huang, W.-Q. Huang, S.-R. Liu, T.-G. Dong, G. Wang, X.-K. Wu, C.-J. Qin, Emission of direct-gap band in germanium with Ge-GeSn layers on one-dimensional structure, Sci Rep. 6 (2016) 24802. https://doi.org/10.1038/srep24802.

[7] S. Wirths, R. Geiger, N. von den Driesch, G. Mussler, T. Stoica, S. Mantl, Z. Ikonic, M. Luysberg, S. Chiussi, J.M. Hartmann, H. Sigg, J. Faist, D. Buca, D. Grützmacher, Lasing in direct-bandgap GeSn alloy grown on Si, Nature Photon. 9 (2015) 88–92. https://doi.org/10.1038/nphoton.2014.321.

[8] R. Loo, Y. Shimura, S. Ike, A. Vohra, T. Stoica, D. Stange, D. Buca, D. Kohen, J. Margetis, J. Tolle, Epitaxial GeSn: impact of process conditions on material quality, Semicond. Sci. Technol. 33 (2018) 114010. https://doi.org/10.1088/1361-6641/aae2f9.

[9] J. Aubin, J.M. Hartmann, A. Gassenq, J.L. Rouviere, E. Robin, V. Delaye, D. Cooper, N. Mollard, V. Reboud, V. Calvo, Growth and structural properties of step-graded, high Sn content GeSn layers on Ge, Semicond. Sci. Technol. 32 (2017) 094006. https://doi.org/10.1088/1361-6641/aa8084.

[10] W. Dou, M. Benamara, A. Mosleh, J. Margetis, P. Grant, Y. Zhou, S. Al-Kabi, W. Du, J. Tolle, B. Li, M. Mortazavi, S.-Q. Yu, Investigation of GeSn Strain Relaxation and Spontaneous Composition Gradient for Low-Defect and High-Sn Alloy Growth, Sci Rep. 8 (2018) 5640. https://doi.org/10.1038/s41598-018-24018-6.

[11] S. Assali, J. Nicolas, O. Moutanabbir, Enhanced Sn incorporation in GeSn epitaxial semiconductors via strain relaxation, Journal of Applied Physics. 125 (2019) 025304. https://doi.org/10.1063/1.5050273.

[12] V. Reboud, A. Gassenq, N. Pauc, J. Aubin, L. Milord, Q.M. Thai, M. Bertrand, K. Guilloy, D. Rouchon, J. Rothman, T. Zabel, F. Armand Pilon, H. Sigg, A. Chelnokov, J.M. Hartmann, V. Calvo, Optically pumped GeSn micro-disks with 16% Sn lasing at 3.1 μ m up to 180 K, Appl. Phys. Lett. 111 (2017) 092101. https://doi.org/10.1063/1.5000353.

[13] D. Rainko, Z. Ikonic, N. Vukmirović, D. Stange, N. von den Driesch, D. Grützmacher, D. Buca, Investigation of carrier confinement in direct bandgap GeSn/SiGeSn 2D and 0D heterostructures, Sci Rep. 8 (2018) 15557. https://doi.org/10.1038/s41598-018-33820-1.

[14] D. Stange, N. von den Driesch, D. Rainko, S. Roesgaard, I. Povstugar, J.-M. Hartmann, T. Stoica, Z. Ikonic, S. Mantl, D. Grützmacher, D. Buca, Short-wave infrared LEDs from GeSn/SiGeSn multiple quantum wells, Optica. 4 (2017) 185. https://doi.org/10.1364/OPTICA.4.000185.
[15] J. Margetis, A. Mosleh, S. Al-Kabi, S.A. Ghetmiri, W. Du, W. Dou, M. Benamara, B. Li, M. Mortazavi, H.A. Naseem, S.-Q. Yu, J. Tolle, Study of low-defect and strain-relaxed GeSn growth via reduced pressure CVD in H2 and N2 carrier gas, Journal of Crystal Growth. 463 (2017) 128–133. https://doi.org/10.1016/j.jcrysgro.2017.01.041.
[16] J. Aubin, J.M. Hartmann, A. Gassenq, L. Milord, N. Pauc, V. Reboud, V. Calvo, Impact of thickness on the structural properties of high tin content GeSn layers, Journal of Crystal Growth. 473 (2017) 20–27. https://doi.org/10.1016/j.jcrysgro.2017.05.006.
[17] J. Margetis, S.-Q. Yu, N. Bhargava, B. Li, W. Du, J. Tolle, Strain engineering in epitaxial $Ge_{1-x}Sn_x$: a path towards low-defect and high Sn-content layers, Semicond. Sci. Technol. 32 (2017) 124006. https://doi.org/10.1088/1361-6641/aa7fc7.
[18] J.M. Hartmann, A. Abbadie, N. Cherkashin, H. Grampeix, L. Clavelier, Epitaxial growth of Ge thick layers on nominal and 6° off Si(0 0 1); Ge surface passivation by Si, Semicond. Sci. Technol. 24 (2009) 055002. https://doi.org/10.1088/0268-1242/24/5/055002.
[19] J.M. Hartmann, A. Abbadie, J.P. Barnes, J.M. Fédéli, T. Billon, L. Vivien, Impact of the H2 anneal on the structural and optical properties of thin and thick Ge layers on Si; Low temperature surface passivation of Ge by Si, Journal of Crystal Growth. 312 (2010) 532–541. https://doi.org/10.1016/j.jcrysgro.2009.11.056.
[20] J.M. Hartmann, A.M. Papon, V. Destefanis, T. Billon, Reduced pressure chemical vapor deposition of Ge thick layers on Si(001), Si(011) and Si(111), Journal of Crystal Growth. 310 (2008) 5287–5296. https://doi.org/10.1016/j.jcrysgro.2008.08.062.
[21] J. Aubin, J.M. Hartmann, GeSn growth kinetics in reduced pressure chemical vapor deposition from Ge2H6 and SnCl4, Journal of Crystal Growth. 482 (2018) 30–35. https://doi.org/10.1016/j.jcrysgro.2017.10.030.
[22] R. Khazaka, E. Nolot, J. Aubin, J.-M. Hartmann, Growth and characterization of SiGeSn pseudomorphic layers on 200 mm Ge virtual substrates, Semicond. Sci. Technol. 33 (2018) 124011. https://doi.org/10.1088/1361-6641/aaea32.
[23] R. Khazaka, J. Aubin, E. Nolot, J.-M. Hartmann, Investigation of the Growth of Si-Ge-Sn Pseudomorphic Layers on 200 mm Ge Virtual Substrates: Impact of Growth Pressure, HCl and Si_2H_6 Flows, ECS Trans. 86 (2018) 207–218. https://doi.org/10.1149/08607.0207ecst.
[24] J. Kraxner, M. Schäfer, O. Röschel, G. Kothleitner, G. Haberfehlner, M. Paller, W. Grogger, Quantitative EDXS: Influence of geometry on a four detector system, Ultramicroscopy. 172 (2017) 30–39. https://doi.org/10.1016/j.ultramic.2016.10.005.
[25] D. Cooper, T. Denneulin, N. Bernier, A. Béché, J.-L. Rouvière, Strain mapping of semiconductor specimens with nm-scale resolution in a transmission electron microscope, Micron. 80 (2016) 145–165. https://doi.org/10.1016/j.micron.2015.09.001.
[26] J.-L. Rouviere, A. Béché, Y. Martin, T. Denneulin, D. Cooper, Improved strain precision with high spatial resolution using nanobeam precession electron diffraction, Appl. Phys. Lett. 103 (2013) 241913. https://doi.org/10.1063/1.4829154.
[27] L. Henry, N. Bernier, M. Jacob, G. Navarro, L. Clément, J.-L. Rouvière, E. Robin, Studying phase change memory devices by coupling scanning precession electron diffraction and energy dispersive X-ray analysis, Acta Materialia. 201 (2020) 72–78. https://doi.org/10.1016/j.actamat.2020.09.033.
[28] M.J. Hÿtch, E. Snoeck, R. Kilaas, Quantitative measurement of displacement and strain fields from HREM micrographs, Ultramicroscopy. 74 (1998) 131–146. https://doi.org/10.1016/S0304-3991(98)00035-7.

[29] J.L. Rouvière, A. Mouti, P. Stadelmann, Measuring strain on HR-STEM images: application to threading dislocations in Al $_{0.8}$ In $_{0.2}$ N, J. Phys.: Conf. Ser. 326 (2011) 012022. https://doi.org/10.1088/1742-6596/326/1/012022.
[30] E. Robin, Method for studying a zone of an object so as to determine a mass-thickness and a composition thereof by using an electron beam and measurements of x-ray radiation intensity, 2016/0169668 A1, 2017.
[31] M. Watanabe, D.B. Williams, The quantitative analysis of thin specimens: a review of progress from the Cliff-Lorimer to the new zeta-factor methods, J Microsc. 221 (2006) 89–109. https://doi.org/10.1111/j.1365-2818.2006.01549.x.
[32] J. Chrétien, N. Pauc, F. Armand Pilon, M. Bertrand, Q.-M. Thai, L. Casiez, N. Bernier, H. Dansas, P. Gergaud, E. Delamadeleine, R. Khazaka, H. Sigg, J. Faist, A. Chelnokov, V. Reboud, J.-M. Hartmann, V. Calvo, GeSn Lasers Covering a Wide Wavelength Range Thanks to Uniaxial Tensile Strain, ACS Photonics. 6 (2019) 2462–2469. https://doi.org/10.1021/acsphotonics.9b00712.
[33] J. Margetis, A. Mosleh, S.A. Ghetmiri, S. Al-Kabi, W. Dou, W. Du, N. Bhargava, S.-Q. Yu, H. Profijt, D. Kohen, R. Loo, A. Vohra, J. Tolle, Fundamentals of Ge 1−x Sn x and Si y Ge 1−x-y Sn x RPCVD epitaxy, Materials Science in Semiconductor Processing. 70 (2017) 38–43. https://doi.org/10.1016/j.mssp.2016.12.024.
[34] M. de la Mata, C. Magén, P. Caroff, J. Arbiol, Atomic Scale Strain Relaxation in Axial Semiconductor III–V Nanowire Heterostructures, Nano Lett. 14 (2014) 6614–6620. https://doi.org/10.1021/nl503273j.
[35] H.V. Stanchu, A.V. Kuchuk, Y.I. Mazur, J. Margetis, J. Tolle, S.-Q. Yu, G.J. Salamo, Strain suppressed Sn incorporation in GeSn epitaxially grown on Ge/Si(001) substrate, Appl. Phys. Lett. 116 (2020) 232101. https://doi.org/10.1063/5.0011842.
[36] A. Elbaz, R. Arefin, E. Sakat, B. Wang, E. Herth, G. Patriarche, A. Foti, R. Ossikovski, S. Sauvage, X. Checoury, K. Pantzas, I. Sagnes, J. Chrétien, L. Casiez, M. Bertrand, V. Calvo, N. Pauc, A. Chelnokov, P. Boucaud, F. Boeuf, V. Reboud, J.-M. Hartmann, M. El Kurdi, Reduced Lasing Thresholds in GeSn Microdisk Cavities with Defect Management of the Optically Active Region, ACS Photonics. 7 (2020) 2713–2722. https://doi.org/10.1021/acsphotonics.0c00708.
[37] J. Chrétien, Q.M. Thai, M. Frauenrath, L. Casiez, A. Chelnokov, V. Reboud, J.M. Hartmann, M. El Kurdi, N. Pauc, V. Calvo, Room temperature optically pumped GeSn microdisk lasers, Appl. Phys. Lett. 120 (2022) 051107. https://doi.org/10.1063/5.0074478.
[38] Y. Zhou, H. Tran, S.-Q. Yu, Development of SiGeSn Technique towards Integrated Mid-Infrared Photonics Applications, (n.d.) 5.
[39] P. Moontragoon, Z. Ikonić, P. Harrison, Band structure calculations of Si–Ge–Sn alloys: achieving direct band gap materials, Semicond. Sci. Technol. 22 (2007) 742–748. https://doi.org/10.1088/0268-1242/22/7/012.
[40] M.J. Hÿtch, J.-L. Putaux, J.-M. Pénisson, Measurement of the displacement field of dislocations to 0.03 Å by electron microscopy, Nature. 423 (2003) 270–273. https://doi.org/10.1038/nature01638.
[41] Y. Wang, P. Ruterana, The strain models of misfit dislocations at cubic semiconductors hetero-interfaces, Appl. Phys. Lett. 103 (2013) 102105. https://doi.org/10.1063/1.4820385.
[42] M. Bertrand, Q.-M. Thai, J. Chrétien, N. Pauc, J. Aubin, L. Milord, A. Gassenq, J.-M. Hartmann, A. Chelnokov, V. Calvo, V. Reboud, Experimental Calibration of Sn-Related Varshni Parameters for High Sn Content GeSn Layers, ANNALEN DER PHYSIK. 531 (2019) 1800396. https://doi.org/10.1002/andp.201800396.
[43] L. Peng, X. Li, J. Zheng, X. Liu, M. Li, Z. Liu, C. Xue, Y. Zuo, B. Cheng, Room-temperature direct-bandgap electroluminescence from type-I GeSn/SiGeSn multiple quantum wells for 2 μm LEDs, Journal of Luminescence. 228 (2020) 117539. https://doi.org/10.1016/j.jlumin.2020.117539.

7. Appendix

Appendix A

One characteristic of Precession Electron Diffraction (PED) is its ability to clearly identify the presence of dislocations whose deformation field in the plane perpendicular to beam direction is not null. As seen in **Figure 2g**, the dislocations induced a strong change from positive to negative rotation component of the crystal. To qualitatively visualize the distribution of dislocations in the structure, a Sobel (i.e. 2D first derivative) filter was applied on the rotation maps in order to identify the center of rotation modification. The sharp change of rotation direction will hence be highlighted, as shown by **Figure S.A**. For relative comparison between samples, the profiles shown in **Figure 3c** and **f** were obtained by normalization of the Sobel image and projection along the growth-plane direction (X vector on **Figure S.A**), which results in the relative dislocation density distribution along the stack.

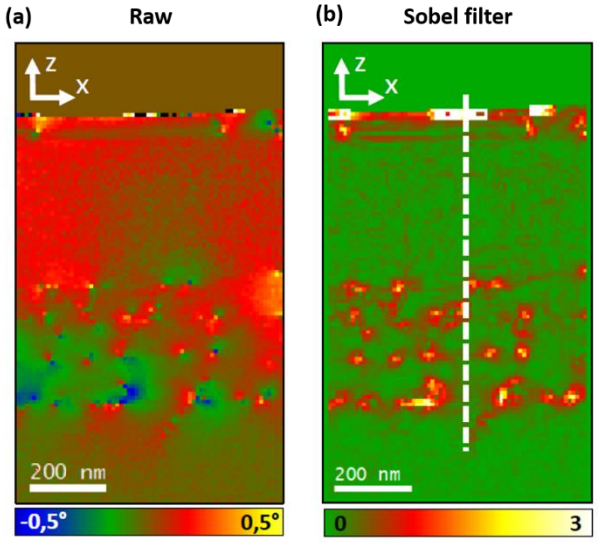

Figure S.A. Comparison between (a) raw rotation map obtained from PED and (b) with a Sobel filter applied, from SG sample analysis.